Chemical Science

ROYAL SOCIETY OF CHEMISTRY

EDGE ARTICLE

View Article Online
View Journal | View Issue

Check for updates

Cite this: *Chem. Sci.*, 2020, **11**, 1649

All publication charges for this article have been paid for by the Royal Society of Chemistry

An intelligent ZIF-8-gated polydopamine nanoplatform for *in vivo* cooperatively enhanced combination phototherapy†

Jie Feng,‡[ab] Wenqian Yu,‡[a] Zhen Xu[a] and Fuan Wang *[a]

The extreme complexity and heterogeneity of fatal tumors requires the development of combination phototherapy considering the limited therapeutic efficiency of conventional monomodal photodynamic therapy (PDT) or photothermal therapy (PTT). However, tumor-specific drug administration and the accompanying hypoxia-restrained PDT present the main obstacles for executing an efficient combination phototherapy. Developing a highly biocompatible, tumor-specific, near infrared absorbing, and oxygen (O_2)-evolving multifunctional nanoplatform is thus crucial for an effective PDT-based combination therapy. In this contribution, a multifunctional ZIF-8-gated polydopamine nanoparticle (PDA) carrier was synthesized for simultaneously delivering a photosensitizer and a catalase (CAT) into tumor cells, thus realizing a cooperatively enhanced combination photodynamic and photothermal therapy, as systematically demonstrated *in vitro* and *in vivo*. The ZIF-8 gatekeeper facilitates the simultaneous and effective delivery of these functional payloads, and the subsequent tumor acidic pH-stimulated drug release. This leads to a significant improvement of combination efficacy by ameliorating tumor hypoxic conditions since the CAT-mediated self-sufficient O_2 generation could substantially promote an efficient PDT operation. In addition, this nanoplatform can effectively convert near infrared photoradiation into heat, resulting in thermally induced elimination of cancerous cells. As an intelligent multi-mode therapeutic nanosystem, this inorganic/organic hybrid nanosystem showed great potential for accurate cancer diagnosis and immediate therapy.

Received 15th December 2019
Accepted 31st December 2019

DOI: 10.1039/c9sc06337d

rsc.li/chemical-science

Introduction

Combination therapy is based on the simultaneous or sequential execution of two or more different types of therapies, and offers a promising avenue for effective cancer treatment since the performance of these therapies could be cooperatively enhanced after a sophisticated integration. Among these different multimodal combination therapies, integrated photodynamic therapy (PDT) and photothermal therapy (PTT) represents the most promising strategy for ablating tumors with minimized side effects. The construction of a multifunctional nanoplatform with integrated PDT and PTT could enhance the therapeutic performance of the corresponding monotherapy.[1–6] However, the oxygen (O_2)-dependent PDT of combination phototherapy usually showed unsatisfying therapeutic effects on hypoxic solid tumors because of the inadequate O_2 supply in tumor vascular systems.[7–13] Another key restraint of potent combination phototherapy originates from lacking specificity towards hypoxic tumor tissue administration, resulting in nonspecific responsibility for causing undesired damage of adjacent healthy tissues.[14–17] Therefore, new nanocarriers and strategies are highly desirable to overcome these obstacles for improving the performance of PDT-based combination therapeutics. To date, several O_2-evolving nanocarriers have been developed with pH-activated photosensitizers for individual PDT.[18,19] However, less work has been devoted to the enhancement of PDT-based combination therapy with an inherent therapeutic photothermal agent and tumor-specific drug administration, as well as the accompanying hypoxia amelioration *via* efficient O_2 generation from endogenous hydrogen peroxide (H_2O_2).

To address these challenges, herein we developed a compact and biocompatible multifunctional phototherapeutic nanomedicine that can selectively release photosensitizers and continuously generate O_2 for cooperatively promoting cancer-specific therapy. ZIF-8-capped polydopamine nanoparticles (PDAs) are designed for encapsulating a photosensitizer, methylene blue (MB), and a catalase (CAT) with high efficiency.

[a]*Key Laboratory of Analytical Chemistry for Biology and Medicine (Ministry of Education), College of Chemistry and Molecular Sciences, Wuhan University, Wuhan 430072, P. R. China. E-mail: fuanwang@whu.edu.cn*

[b]*College of Chemistry, Chemical Engineering and Materials Science, Collaborative Innovation Center of Functionalized Probes for Chemical Imaging in Universities of Shandong, Key Laboratory of Molecular and Nano Probes, Ministry of Education, Shandong Normal University, Jinan 250014, P. R. China*

† Electronic supplementary information (ESI) available. See DOI: 10.1039/c9sc06337d

‡ These authors contributed equally to this work.

The ZIF-8 shell acts as a smart gatekeeper for simultaneously facilitating an effective delivery of the photosensitizer and CAT into tumor tissues, where the tumor microenvironment-stimulated release of these therapeutic agents ameliorates tumor hypoxic conditions and improves PDT-based combination therapy efficacy, as systematically demonstrated *in vitro* and *in vivo*. More importantly, this intelligent "gatekeeper" can be further designed to integrate more versatile functions, for example, stimuli-enhanced diagnostic imaging for a comprehensive learning of the initial biodistribution and the subsequent therapeutic response of nanomedicine, and the accurate location and morphology of tumors, thus broadening the scope of synergistic phototherapy for smart and accurate diagnosis-guided immediate and cooperative phototherapy applications.

Results and discussion

Principle of the intelligent ZIF-8-gated combinational photodynamic and photothermal therapy

As illustrated in Scheme 1, the compact inorganic–organic hybrid PDAs-ZIF-8 (PZ) nanoparticles were prepared *via* a simple *in situ* and sequential growth procedure. A heterogeneous nucleation and growth of a ZIF-8 shell was realized on a PDA surface and was attributed to the metal-chelating ability of catechol groups of PDAs with the superficial metal ions of ZIF-8.[20,21] However, large molecules cannot enter the pores of ZIF-8 because the diameter of the pores of ZIF-8 is 3.4 Å. However, hierarchical structures can always be introduced into MOFs, which may lead to an increased loading of different guest molecules.[22–25] Hence, the porous structure of ZIF-8 enabled its efficient encapsulation of different molecules, *e.g.*, MB and CAT, during the one-pot assembly process, resulting in the multifunctional PDAs-MB-CAT-ZIF-8 (PMCZ) nanoparticles. The as-synthesized PMCZ could be specifically accumulated in tumor tissue *via* a well-known enhanced permeability and retention (EPR) effect and subsequently uptaken by the corresponding cancer cells. Once PMCZ enters into cytoplasm, it exhibits a tumor acidic pH-triggered release of MB and CAT payloads. The released CAT then catalyzes the decomposition of H_2O_2 into O_2 that can promote the MB-sensitized O_2-dependent PDT through this hypoxia amelioration strategy. In addition, the compact PDA-involved hybrid nanocarrier is endowed with near-infrared PTT character, thus enabling the synergetic combined photodynamic–photothermal therapy *in vitro* and *in vivo*.

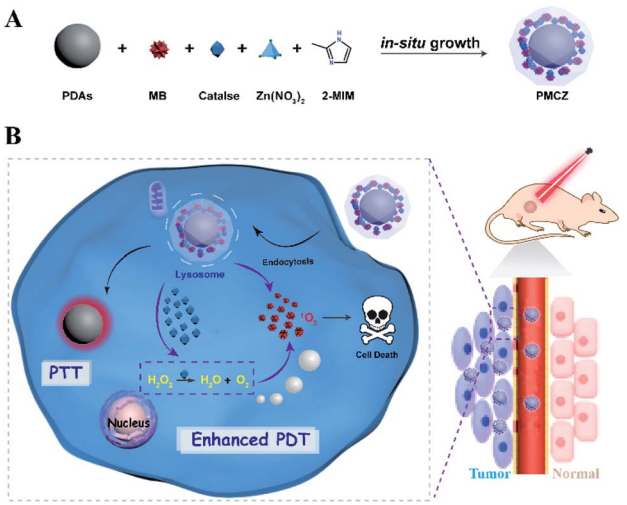

Scheme 1 Schematic illustration of the construction and the subsequent administration of the intelligent ZIF-8-gated PDA nanohybrids for enhancing the anticancer activity of combined photodynamic and photothermal therapy.

Synthesis and characterization of the PMCZ nanoplatform

As shown in Fig. 1A, the morphologies of PDAs and PMCZ were characterized by transmission electron microscopy (TEM) and scanning electron microscopy (SEM). Compared with the bare PDAs, an obviously rough surface was observed for PMCZ with an average size increment of 20 nm, which was consistent with its hydrodynamic diameter change as measured by dynamic light scattering (DLS) (Fig. 1B), indicating that the ZIF-8 shell was successfully assembled on the surface of PDAs. The zeta potential of PMCZ shifted from −30.1 mV to 13.2 mV due to the modification of the positively charged ZIF-8 outer layer. Powder X-ray diffraction (PXRD) also evidenced the successful deposition of ZIF-8, and the crystal structure of ZIF-8 was not influenced by the encapsulated MB and CAT (Fig. 1C). The color of the supernatant changed from blue to colorless after several washing steps, indicating that MB molecules were indeed encapsulated and efficiently locked in the PMCZ nanohybrids (Fig. S1†). Next, sodium dodecyl sulfate-polyacrylamide gel electrophoresis (SDS-PAGE) revealed a characterized band of CAT (molecular weight, 60 kDa) from PMCZ, verifying the successful encapsulation of CAT into PMCZ (Fig. 1D). Besides, thermal gravimetric analysis

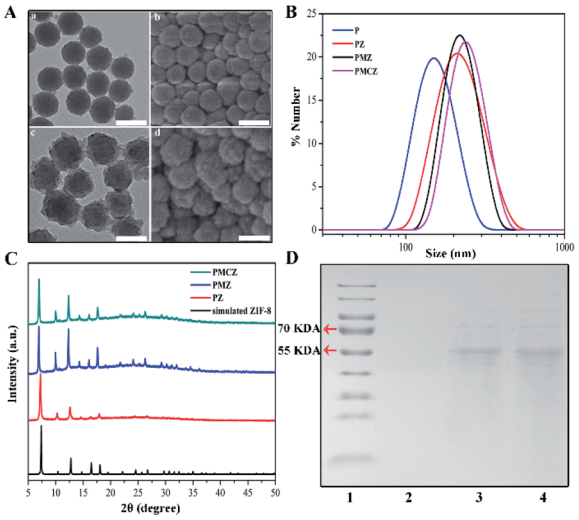

Fig. 1 Characterization of the PDAs-MB-CAT-ZIF-8 (PMCZ) nanoparticles. (A) TEM and SEM images of PDAs (a, b) and PMCZ (c, d), respectively. Scale bar, 100 nm. (B) Size distributions of PDAs (P), PDAs-ZIF-8 (PZ), PDAs-MB-ZIF-8 (PMZ) and PMCZ nanostructures. (C) XRD patterns of the simulated ZIF-8, PZ, PMZ and PMCZ nanohybrids. (D) SDS-PAGE analysis of the corresponding protein from marker (1), PMZ (2), PMCZ (3) and free catalase (CAT, 4).

(TGA, Fig. S2†) and fourier transform infrared spectroscopy (FI-TR, Fig. S3†) further demonstrated the efficient embedment of MB and CAT in PMCZ. The thermogravimetric analysis (TGA) of PMCZ nanomedicine shows a faster thermal degradation rate above ~320 °C than the other ZIF-8-involved nanohybrids (Fig. S2†). This is attributed to the decomposition of catalase payloads in PMCZ, which is in agreement with the reported literature.[26,27] The FT-IR spectra of PMCZ revealed two characteristic FI-TR peaks of MB (1393 and 1530 cm^{-1}) after the encapsulation of MB into ZIF-8 (Fig. S3†), which are due to the C=N and $-CH_3$ symmetric deformation, demonstrating the efficient loading of MB into PMCZ. On the other hand, a new FT-IR peak emerging at 1688 cm^{-1} corresponded to the amide I (Fig. S3†), demonstrating an efficient encapsulation of the CAT payload. The respective loading capacity of CAT and MB was calculated to be 3.4% and 5% based on the following procedure. After the loading of CAT and MB molecules into ZIF-8 and the subsequent centrifugation and H_2O-washing procedures, the supernatant was collected to measure the un-encapsulated guest molecules. According to the standard curve of a commercially standard BSA protein (Fig. S4†) and the same MB molecule (Fig. S5†), and the corresponding calibration curve and equation, the loading capacity of CAT or MB was calculated as follows: Loading capacity (%) = $(M - M_1)/M_2 \times 100\%$, where M represents the initial feeding amount of CAT or MB, M_1 represents the CAT or MB content of the supernatant, and M_2 represents the content of PMCZ. Not surprisingly, the BCA-based CAT encapsulation efficiency (~3.5% (wt)) was consistent with that obtained using the TGA-involved calculation method (~3.5% (wt)). The Uv-vis-NIR absorption spectra of PMCZ showed a broad absorption band ranging from ultraviolet (UV) to near-infrared (NIR) regions (Fig. S6†), indicating that PMCZ was a good photothermal agent for facilitating PTT operation. Besides, the characteristic peak of methylene blue (MB) at 663 nm was retained, which guarantees its potential photodynamic performance.

Tumor-responsive MB release, photodynamic and photothermal therapeutic performances of the PMCZ nanosystem

To investigate the controlled release behavior of the MB payload, the PMCZ nanoparticles were incubated in different buffers with varied pH. The released MB could be quantified by its fluorescence and the corresponding standard calibration curve (Fig. S5†). As shown in Fig. 2A, the loaded MB was nearly unreleased at pH 7.4, yet showed an obviously sustained release from PMCZ at pH 5.0. After 25 h of incubation, 15% and 60% of MB were released at pH 7.4 and pH 5.0, respectively. It was attributed to the fact that the ZIF-8 gatekeeper remained stable under neutral conditions while degraded easily under acidic stimulus, thus releasing the encapsulated payloads in an acidic tumor microenvironment. Taken together, this PMCZ nanosystem would be considered as a promising drug delivery carrier for enhancing MB accumulation in tumor tissue without premature release under normal physiological conditions.

Under 660 nm photoirradiation, the released MB could be utilized as an efficient PDT photosensitizer for generating

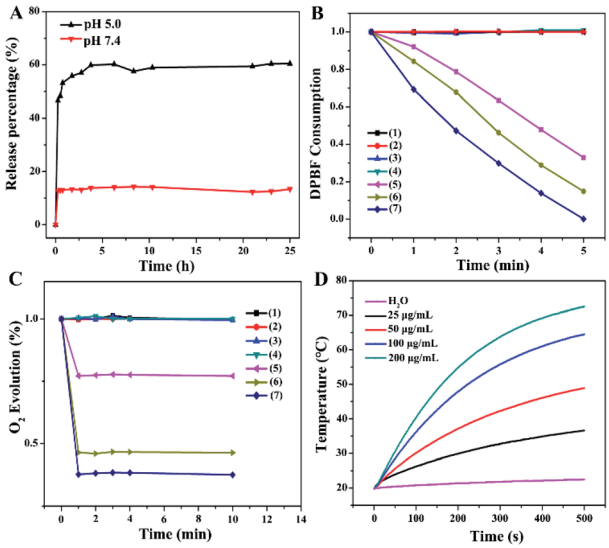

Fig. 2 *In vitro* evaluation of MB release, O_2 generation, photodynamic and photothermal performance of PMCZ. (A) Time-dependent release profiles of MB from PMCZ (50 μg mL^{-1}) at different external pH stimuli. (B) $^1O_2$ production efficiency of the different samples with different treatments. (1) DPBF; (2) DPBF and 660 nm photoirradiation (100 mW cm^{-2}); (3) DPBF and H_2O_2 (100 μM); (4) DPBF, H_2O_2 (100 μM) and 660 nm photoirradiation (100 mW cm^{-2}); (5) DPBF and PMCZ (50 μg mL^{-1}) at pH 7.4; (6) DPBF and PMCZ (50 μg mL^{-1}) at pH 5.0; (7) DPBF, PMCZ (50 μg mL^{-1}) and H_2O_2 (100 μM) at pH 5.0. (C) O_2 generation of these different samples after being incubated with RDPP under different conditions. (1) H_2O_2 (100 μM); (2) H_2O_2 (100 μM) and PDAs (50 μg mL^{-1}); (3) H_2O_2 (100 μM) and PZ (50 μg mL^{-1}); (4) H_2O_2 (100 μM) and PMZ (50 μg mL^{-1}); (5) H_2O_2 (100 μM) and PMCZ (50 μg mL^{-1}); (6) H_2O_2 (500 μM) and PMCZ (50 μg mL^{-1}); (7) H_2O_2 (1000 μM) and PMCZ (50 μg mL^{-1}). (D) Heating curves of PMCZ with different concentrations upon 808 nm photoirradiation (2 W cm^{-2}).

singlet oxygen ($^1O_2$) that was responsible for PDT-motivated cell death. To investigate the PDT effect, 1,3-diphenylisobenzofuran (DPBF), an indicator of ROS, was used to evaluate the PMCZ-generated $^1O_2$ under different physiological conditions.[28,29] As shown in Fig. 2B, the as-obtained PMCZ exhibited a sharp 80% decline of DPBF absorbance under 660 nm photoirradiation at pH 5.0 for 5 min. Conversely, the absorbance of DPBF decreased to 50% at pH 7.4, indicating an enhanced $^1O_2$ generation in an acidic environment. This is attributed to the released MB that mediates the efficient photo-catalyzed $^1O_2$ generation from the surrounding O_2-containing environment. In addition, the concomitantly released CAT could further catalyze the decomposition of H_2O_2 for generating O_2, which was beneficial for enhancing the O_2-dependent PDT. Firstly, we assessed the PMCZ-responsive O_2 generation from H_2O_2 by using an O_2 probe, $[Ru(dpp)_3]Cl_2$ (RDPP), whose fluorescence could be quenched by O_2. After the incubation of PMCZ with H_2O_2, the fluorescence of RDPP was quenched immediately within 2 min and kept constant for 8 min (Fig. 2C). And the fluorescence of RDPP decreased with increasing concentration of H_2O_2, implying that the as-generated O_2 was indeed originated from the decomposition of H_2O_2. In contrast, PMCZ showed a negligible fluorescence change without H_2O_2. Similar results were

observed in the PDAs-MB-ZIF-8 (PMZ) group, further verifying that the O_2 generation was resulted from PMCZ-embedded CAT-catalyzed decomposition of H_2O_2. Secondly, the PMCZ-mediated generation of $^1O_2$ was promoted by H_2O_2-involved O_2 evolution. It is more interpretable since the O_2 obtained by CAT-mediated generation could be further converted into $^1O_2$ by the supplement H_2O_2. As expected, a more distinctly decreased DPBF absorption was observed upon the addition of H_2O_2 into PMCZ (Fig. 2B), confirming that the O_2 generation could substantially reinforce the PDT effect of our PMCZ system.

Due to the excellent photothermal conversion of the PDA constituent, we next investigated the photothermal performances of the compact PMCZ nanohybrid by exposing it to 808 nm NIR laser at a fixed laser power density (2 W cm^{-2}). Pure water was used as the negative control. As shown in Fig. 2D, the temperature of the PMCZ solution increased with elevated concentration or irradiation duration. For example, the temperature of PMCZ increased by 50 °C after NIR irradiation for 500 s. In comparison, the temperature change of pure water was negligible (2.8 °C). Besides, a similar temperature change was obtained for both of PMCZ and PDAs, indicating that it was the PDAs that mediated the efficient photothermal conversion and the ZIF-8 gatekeeper did not influence the photothermal effect of PDAs (Fig. S7†). The robust and efficient photothermal conversion of PMCZ was further revealed by the repeated temperature changes during the five successive laser irradiation on/off cycles (Fig. S8†), which are attributed to the intrinsic photothermal feature of the PDA constituent. Collectively, these results suggested that PMCZ would be considered as a promising photothermal agent for executing an efficient anticancer therapy.

Demonstration of the formation of the PMCZ nanoplatform

Although all these results have confirmed that the CAT and MB are simultaneously loaded into PMCZ, it is unclear where these MB and CAT guest molecules are exactly loaded in PDAs or ZIF-8. First of all, ZIF-8 can be *in situ* loaded with many molecules, including proteins (*e.g.*, enzymes), small molecules (*e.g.*, dyes) and so on, according to the reported literatures.[29–32] Meanwhile, the metal-chelating activity of PDA catechol groups can drive the heterogeneous nucleation and growth of ZIF-8 coatings on PDA nanoparticles, affording exclusively the assembly of the sophisticated core–shell nanohybrids.[20,21] Based on the above two considerations, we hypothesized that MB and CAT can be simultaneously embedded into ZIF-8 during the growth of ZIF-8 on PDAs. Secondly, the optimization of the synthetic procedure also demonstrated the underlying inter-component (PDAs-ZIF-8) interactions. The PMCZ structure could not be formed by changing the adding sequence of $Zn(NO_3)_2$ and 2-methylimidazole (2-MIM). Thus the metal-chelation between the ZIF-8 zinc constituent and PDA catechol groups plays a dominating role in this synthesis process. Besides ZIF-8, PDAs could also adsorb partial MB and CAT on their surface. Yet the MB and CAT were mainly encapsulated in the ZIF-8 shell based on the following experimental demonstrations. By dissolving the outer layer of ZIF-8 and its encapsulated molecules, these PDA surface-adsorbed MB and CAT were determined to be 2.5% and 1.4%, respectively, once the PMCZ-loaded MB and CAT were both assumed to be 100%. Obviously, these PDA surface-anchored MB and CAT were so little that they can be negligible. The gatekeeper function of ZIF-8 was based on the following experimental demonstrations: Firstly, the controlled MB release behavior of PMCZ is different in different pH buffers. The loaded MB was nearly unreleased at pH 7.4, yet showed an obviously sustained release from PMCZ at pH 5.0 (Fig. 2A). It was attributed to the fact that ZIF-8 remained stable under neutral conditions while degraded easily under acidic stimulus. Clearly, MB is loaded into ZIF-8, otherwise the release rate could not be differentiated. On the other hand, the amount of PMCZ-generated O_2 in an acidic H_2O_2 microenvironment was larger than that under neutral H_2O_2 conditions, further confirming that CAT is loaded into the ZIF-8 layer.

Cellular uptake of the PMCZ nanosystem

In order to study the cellular uptake of PMCZ, the PMCZ-treated HeLa cells were used for acquiring confocal laser scanning microscopy (CLSM) images. Obviously, a stronger red fluorescence was obtained from PMCZ-treated cells (sample 2, Fig. 3A) as compared with that from the control cells (sample 1, Fig. 3A), illustrating that PMCZ could be effectively internalized by HeLa cells after 4 h. Then an oxidation-sensitive probe, 2′, 7′-dichlorofluorescein diacetate (DCFH-DA), was employed to determine the intracellular ROS generation in HeLa cells. DCFH-DA could be oxidized by ROS to generate dichlorofluorescein (DCF) with bright green fluorescence. The intact and 660 nm photoirradiated HeLa cells showed no fluorescence of DCF (samples 1 and 2 of Fig. 3B, respectively), indicating that no ROS has been generated in these samples. As compared with PMZ-treated HeLa cells (sample 3 of Fig. 3B), a strong green fluorescence was observed in 660 nm photoirradiated PMZ-treated HeLa cells (sample 5 of Fig. 3B), indicating that PMZ is capable of generating ROS under laser irradiation. Furthermore, the CAT-encapsulating PMCZ-treated cells (sample 4 of Fig. 3B) showed a much higher intracellular ROS expression after 660 nm photoirradiation (sample 6 of Fig. 3B), indicating that PMCZ-delivered CAT actually acts as an effective O_2 promotor for increasing ROS generation. To prove this mechanism, RDPP was used to qualitatively evaluate intracellular O_2 generation (Fig. 3C). The intact and CAT-absent PMZ-treated cells revealed a stronger green fluorescence (lower O_2 content, samples 1 and 2 of Fig. 3C, respectively), while the PMCZ groups displayed a weaker fluorescence of RDPP (higher O_2 content, sample 3 of Fig. 3C). Obviously, it was the PMCZ-encapsulated CAT that promoted the efficient intracellular O_2 generation. All of these demonstrate that PMCZ could effectively ameliorate the hypoxic tumor microenvironment by CAT-generated O_2 *in situ* from endogenous H_2O_2.

In vitro cytotoxicity and therapeutic investigation of the PMCZ nanoplatform

To investigate the *in vitro* cooperatively enhanced combined photothermal and photodynamic therapy, the cytotoxicity of

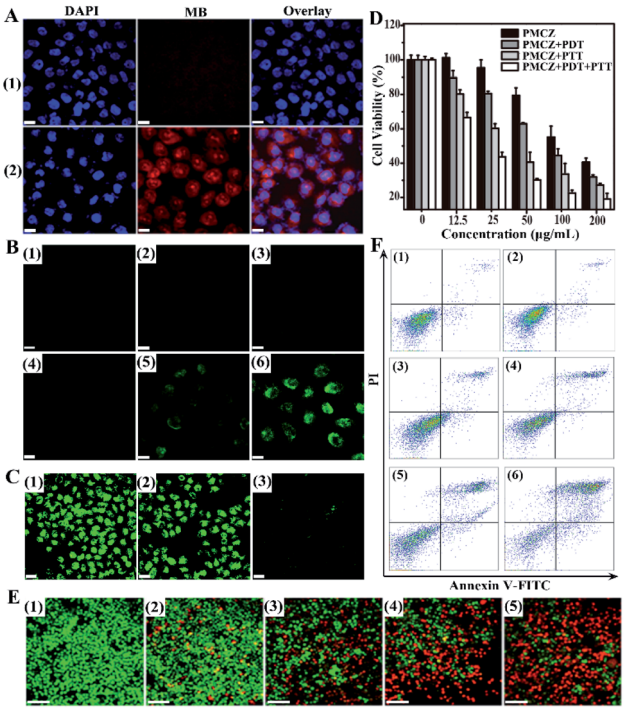

Fig. 3 *In vitro* anti-tumor efficacy of PMCZ nanomedicine. (A) Intracellular imaging of PMCZ (50 μg mL^{-1})-treated HeLa cells for 4 h. (B) CLSM images of intracellular ROS generation from intact HeLa cells (1), cancer cells with 660 nm photoirradiation (100 mW cm^{-2}) (2), PMZ (50 μg mL^{-1}) (3), PMCZ (50 μg mL^{-1}) (4), PMZ (50 μg mL^{-1}) with PDT (100 mW cm^{-2}) (5), and PMCZ (50 μg mL^{-1}) with PDT (100 mW cm^{-2}) (6). (C) CLSM images of intracellular O_2 generation from HeLa cells after 4 h of RDPP incubation with different treatments: Intact HeLa cells (1), PMZ (50 μg mL^{-1})-treated cancer cells (2), and PMCZ (50 μg mL^{-1}) treated cells (3). (D) Viability of HeLa cells after their incubation with varied concentrations of PMCZ and photoirradiation (660 nm, 100 mW cm^{-2} or 808 nm, and 2 W cm^{-2}). (E) Intracellular imaging of calcein AM/PI co-stained HeLa cells with different treatments: intact HeLa cells (1), PMCZ (50 μg mL^{-1})-treated cells (2), PMCZ (50 μg mL^{-1}) + PDT (660 nm, 100 mW cm^{-2}) (3), PMCZ (50 μg mL^{-1}) + PTT (808 nm, 2 W cm^{-2}) (4) and PMCZ (50 μg mL^{-1}) + PDT (660 nm, 100 mW cm^{-2}) + PTT (808 nm, 2 W cm^{-2}) (5). Scale bar, 50 μm. (F) Flow cytometric analysis of differently treated HeLa cells after Annexin V and FITC-PI staining, intact HeLa cells (1), PMCZ (50 μg mL^{-1})-treated cells (2), PMCZ (50 μg mL^{-1}) + PDT (660 nm, 100 mW cm^{-2}) (3), PMCZ (50 μg mL^{-1}) + PTT (808 nm, 2 W cm^{-2}) (4), PMZ (50 μg mL^{-1}) + PDT (660 nm, 100 mW cm^{-2}) + PTT (808 nm, 2 W cm^{-2}) (5) and PMCZ (50 μg mL^{-1}) + PDT (660 nm, 100 mW cm^{-2}) + PTT (808 nm, 2 W cm^{-2}) (6). Scale bar, 50 μm.

PMCZ was examined by using the standard methylthiazolyl tetrazolium (MTT) assay for safety, which is a necessary property of nanoparticles for biomedical applications. In the absence of any photoirradiation, no significant cell death was observed in HeLa cells that were treated with different concentrations of PMCZ for 4 h (Fig. S9†), suggesting a good biocompatibility of our PMCZ nanohybrid. Further 660 nm or 808 nm laser irradiation resulted in the decreased viability of HeLa cells, suggesting that the administered PMCZ worked well for photothermal and photodynamic ablation of cancer cells. The *in vitro* combination therapy efficacy was estimated by comparing the viability of HeLa cells that were treated with PMCZ + PDT, PMCZ + PTT and PMCZ + PDT + PTT, respectively (Fig. 3D). Clearly, the cytotoxicity of PMCZ + PDT + PTT dramatically decreased as compared to that of PMCZ + PDT and PMCZ + PTT groups. The IC50 values of each group were also acquired and summarized in Fig. S10.† As compared with the intact cells, the IC50 value of PMCZ-treated cells was determined to be 157.6 μg mL^{-1}. After 660 nm and 808 nm laser irradiation, the IC50 value of PMCZ-treated cells decreased significantly (23.61 μg mL^{-1}) as compared with those of single PDT (88.88 μg mL^{-1}) or PTT (44.09 μg mL^{-1}) treated cells, demonstrating again the combination anti-tumor efficacy of this compact multifunctional therapy. All these results demonstrated the cooperatively enhanced therapeutic effect between PDT and PTT. Note that the photothermal effect of PMCZ was insignificant under 660 nm laser irradiation, and the current PDT irradiation was not suitable for the PTT system (Fig. S11A†). Similarly, the current PTT irradiation system was not suitable for executing an efficient PDT under 808 nm laser irradiation (Fig. S11B†). For realizing both PTT and PDT effects under the irradiation of these two wavelengths (808 nm and 660 nm), the entrapment of indocyanine green molecule (ICG) dyes into the present PZ nanohybrid might be a possible way to realize an efficient combination phototherapy, considering that ICG is a Food and Drug Administration (FDA)-approved NIR dye, it thus could serve as both photothermal and photodynamic agents.[33–35]

In order to visualize the combination therapy effect, a live/dead cell staining assay was carried out to observe the apoptosis of differently treated cells (Fig. 3E). Here live cells were stained with calcein acetoxymethyl ester (calcein AM) with green fluorescence while dead cells were stained with propidium iodide (PI) with red fluorescence. The intact and PMCZ-treated cells exhibited almost all green fluorescence (samples 1 and 2 of Fig. 3E, respectively), indicating that mere PMCZ could not effectively eliminate cancer cells. With 808 nm or 660 nm laser irradiation (samples 3 and 4 of Fig. 3E, respectively), dead cells appeared with red fluorescence staining due to the PMCZ-generated ROS reagent or heat stimulus. For the PMCZ + PDT + PTT group, all cells were nearly completely destroyed with red fluorescence staining (samples 5 of Fig. 3E). These results were consistent with the MTT assay, revealing the enhanced therapeutic effect of our combined photodynamic and photothermal therapy.

To gain a crucial and in-depth understanding of the PMCZ-mediated cell apoptosis, HeLa cells were examined by using the dual fluorescence of Annexin V-FITC/PI through flow cytometry. As compared with the intact cells (samples 1 of Fig. 3F), the apoptosis percentage of PMCZ-treated cells was determined to be 5.07% (samples 2 of Fig. 3F). After 660 nm and 808 nm laser irradiation, the apoptosis level of PMCZ-treated cells was significantly increased (60.32%, samples 6 of Fig. 3F) as compared with a single PDT (15.50%, samples 3 of Fig. 3F) or PTT (25.01%, samples 4 of Fig. 3F) treatment, supporting again the promoted combination anti-tumor efficacy of this multifunctional therapy. Besides, the apoptosis population of CAT-absent PMZ-treated cells with 660 nm and 808 nm laser irradiation (PMZ + PDT + PTT) was only 30.69% (samples 5 of Fig. 3F), which is much lower

than that of the PMCZ + PDT + PTT group (60.32%, samples 6 of Fig. 3F). Such results indicated that the O_2 generation could reinforce the PDT effect and could also contribute to the improvement of the combination phototherapy.

Overcoming tumor hypoxia *in vivo* by the PMCZ nanosystem

Encouraged by the effective O_2 production from PMCZ, we subsequently investigated its hypoxia amelioration ability by using the immunochemistry assay (Fig. 4A). The untreated tumor cells were stained dark brown (samples 1 of Fig. 4A), demonstrating that the corresponding hypoxia responsive transcription factor (HIF-1α) was overexpressed under tumor hypoxic conditions, which was similar to the PMZ-treated group (samples 2 of Fig. 4A). In contrast, the immunofluorescence of the PMCZ-treated group was much weaker (samples 3 of Fig. 4A), suggesting that the tumor hypoxia is significantly relieved through the CAT-mediated O_2 generation. Additionally, Western blot analysis further demonstrated that the HIF-1α expression was significantly decreased in the PMCZ-treated tumor as compared with that of PMZ (Fig. 4B and C), which was consistent with the previous immunochemistry assay (Fig. 4A). Taken together, these results revealed a high O_2 generation capacity of our PMCZ for ameliorating the hypoxic tumor microenvironment.

In vivo combination therapeutic effect of the smart PMCZ nanosystem

Before investigating the ultimate combination therapeutic PTT/PDT effect, we evaluated the biocompatibility, biodistribution and photothermal effect of PMCZ *in vivo*. Firstly, no hemolysis was detected when red blood cells were incubated with different concentrations of PMCZ (Fig. S12†), illustrating a satisfied blood compatibility of the nanoplatform for further biomedical applications. Subsequently, the distribution of PMCZ in HeLa tumor-bearing mice was measured by inductively coupled plasma atomic emission spectroscopy (ICP) after the tail intravenous injection of PMCZ for different durations (4, 6, 12, 24 and 48 h). An obviously elevated Zn element in the tumor site was observed after 24 h of PMCZ injection (Fig. S13†) while the zinc content decreased with extended injection time, verifying that the "off-target" nanoparticles could be effectively cleared out of the body without long-term physiological toxicity. These results demonstrated the tumor-specific accumulation of our nanomedicine, and provided possibility for examining the *in vivo* antitumor capability of PMCZ. Besides, the *in vivo* imaging system (IVIS) also confirmed that PMCZ was mainly accumulated in the tumor site as compared with liver and spleen organs (Fig. S14†). Besides, PBS and PMCZ were intravenously injected into tumor-bearing mice to investigate their photothermal performance *in vivo*. After 24 h of injection, the tumor was irradiated with 808 nm laser (1.0 W cm^{-2}, 10 min) for recording the temperature of mice using an IR thermal camera. As shown in Fig. 5A and S15,† the temperature of the tumor increased rapidly to 45 °C within 2 min (sample b), which was adequate to

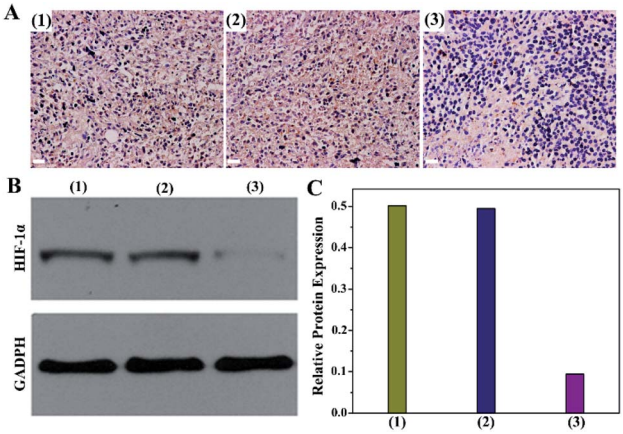

Fig. 4 PMCZ-mediated amelioration of the tumor hypoxic microenvironment. (A) Representative immunochemistry images of HIF-1α in (1) intact tumor tissues, (2) 50 μg mL^{-1} PMZ-treated tumor tissues, and (3) 50 μg mL^{-1} PMCZ-treated tumor tissues. Scale bar, 50 μm. (B) Western blot assay of HIF-1α expression from (1) intact tumor tissues, (2) 50 μg mL^{-1} PMZ-treated tumor tissues, and (3) 50 μg mL^{-1} PMCZ-treated tumor tissues. (C) The corresponding quantitative analysis of (B).

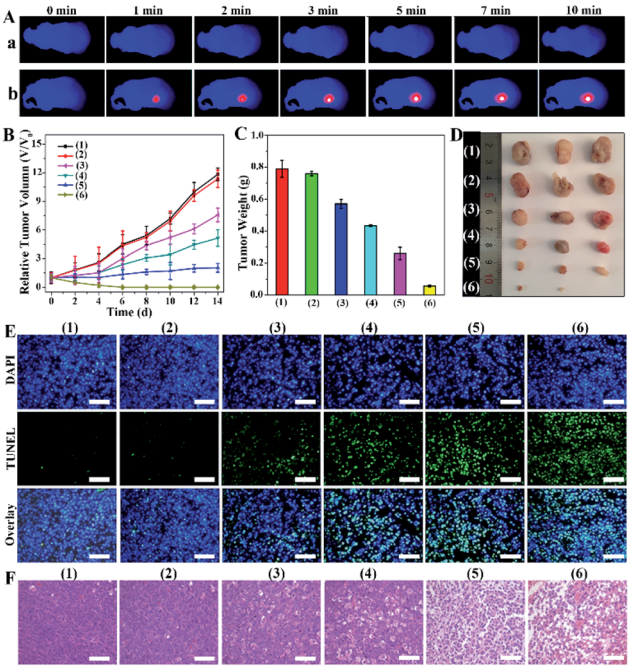

Fig. 5 *In vivo* antitumor efficacy of PMCZ nanoparticles. (A) Thermal IR images of differently treated mice under 808 nm photoirradiation (1 W cm^{-2}) after 24 h post-injection of PBS (50 μL) (a) or PMCZ (50 μL, 800 μg mL^{-1}) (b). (B) Relative tumor volume growth curves and (C) tumor weights of mice after different treatments. (D) Photographs of tumors collected from tumor-bearing mice at the end of each different treatment. (E) H&E and (F) TUNEL stained images of tumor sections from differently treated groups at the end of each anti-tumor study. These groups include PBS (50 μL) (1), PMCZ (50 μL, 800 μg mL^{-1}) (2), PMCZ (50 μL, 800 μg mL^{-1}) + PDT (660 nm, 1 W cm^{-2}) (3), PMCZ (50 μL, 800 μg mL^{-1}) + PTT (808 nm, 1 W cm^{-2}) (4), PMZ (50 μL, 800 μg mL^{-1}) + PDT (660 nm, 1 W cm^{-2}) + PTT (808 nm, 1 W cm^{-2}) (5) and PMCZ (50 μL, 800 μg mL^{-1}) + PDT (660 nm, 1 W cm^{-2}) + PTT (808 nm, 1 W cm^{-2}) (6). Scale bar, 100 μm.

ablate tumor cells. In contrast, the PBS-treated tumor exhibited a slightly lower temperature change (35 °C, sample a), demonstrating the feasibility of our PMCZ for *in vivo* photothermal therapy.

In order to evaluate the antitumor efficacy of PMCZ, the HeLa tumor-bearing mice were randomly divided into six groups for different treatments, *i.e.*, (1) PBS, (2) PMCZ, PMCZ + PDT (3), PMCZ + PTT (4), PMZ + PDT + PTT (5), and PMCZ + PDT + PTT (6). The tumor size was measured each day and these differently treated tumors were harvested for weighing and photographing at the end of 14 day treatment. As shown in Fig. 5B and C, the mice experienced a rapid tumor growth in the PBS or PMCZ treatment, indicating that mere PMCZ had no influence on tumor growth. In comparison, the PMCZ + PDT or PMCZ + PTT group showed a moderate repression of tumor growth, but it still could not thoroughly restrain the tumor growth. The tumors were completely suppressed and even ablated in the PMCZ + PDT + PTT-treated tumor, thus clearly demonstrating the effective PDT/PTT dual-modal therapeutic operation of PMCZ. It should be noted that the therapeutic effect of the PMCZ + PDT + PTT group was higher than that of CAT-absent PMZ + PDT + PTT group, which is attributed to the PMCZ-induced hypoxia amelioration for enhancing the PDT effect in a tumor hypoxic microenvironment. In order to study the underlying mechanism of the enhanced tumor suppression by PMCZ, the western blot assay was carried out to detect the varied expression of antiapoptotic protein (Bcl-2) and proapoptotic protein (capase-3) in tumor tissues (Fig. S16†). Obviously, a maximum extent of Bcl-2 down-regulation and concomitant capase-3 up-regulation was observed in the PMCZ + PTT + PDT group, suggesting that the combination phototherapy induced the highest tumor apoptosis. Subsequently, hematoxylin and eosin (H&E) staining and *in situ* terminal deoxynucleotidyl transferase-mediated dUTP nick end labeling (TUNEL) staining assays were carried out to evaluate the tumor inhibition effect of different treatments (Fig. 5E). The PMCZ-mediated combination PDT/PTT therapy showed the most drastic apoptosis of cancer cells. The histological image of HE assays shows similar results where the PMCZ + PDT + PTT group exhibited a severe nuclear destruction in the corresponding morphology of tumor tissues (Fig. 5F). Taken together, these results validated that PMCZ acted as an effective O_2-supplying nanoplatform for combination phototherapy in a tumor hypoxic microenvironment. In addition, all mice were sacrificed to collect the organs, including heart, liver, spleen, lung and kidneys, and to evaluate the biosafety of our PMCZ from histological analysis. As shown in Fig. S17,† no obvious physiological morphology changes and adverse effects were observed for these different organs. Besides, the body weight of each group had no significant change during these different treatments (Fig. S18†), suggesting no systemic toxicity of the as-constructed PMCZ nanoparticles.

Conclusions

In summary, a cooperatively enhanced phototherapy was established and systematically investigated by integrating a MOF gatekeeper on PDAs. This stimuli-responsive core–shell nanoplatform realized a high MB loading and a self-sufficient O_2 generation, thus achieving a cooperatively enhanced PDT and PTT for effective anti-cancer treatment. The as-achieved PMCZ nanohybrids could be accumulated in tumor sites, where the acidic dissolution of ZIF-8 guarantees the slow release of MB in tumor cells without premature MB exposure to blood or normal physiological conditions. Importantly, our study has demonstrated the feasibility of improving PDT through CAT-enhanced self-sufficient O_2 evolution and the immediate MB-irradiated ROS generation. Furthermore, the superior photothermal efficiency and excellent biocompatibility of PDAs were retained for performing the combined PDT and PTT operations, thus realizing the jointly enhanced therapeutic efficacy for completely obliterating the primary tumors. Our study sheds light on the efficient integration of combination phototherapy and broadens the scope of smart synergistic therapy-based cancer diagnosis and immediate drug administrations.

Conflicts of interest

There are no conflicts to declare.

Acknowledgements

This work is supported by the National Natural Science Foundation of China (21874103, 81602610), National Basic Research Program of China (973 Program, 2015CB932601), and Fundamental Research Funds for the Central Universities (2042018kf0210, 2042018kf1006, and 2042019kf0206). All the animal experiments were performed based on the Principles of the Administration of Affairs Concerning Experimental Animals. The animal protocols used in this study were approved by The Institutional Animal Use and Care Committee of Wuhan University of China.

Notes and references

1 W. Fan, B. Yung, P. Huang and X. Chen, *Chem. Rev.*, 2017, **117**, 13566–13638.
2 J. Pan, X. Zhu, X. Chen, Y. Zhao and J. Liu, *Biomater. Sci.*, 2018, **6**, 372–387.
3 L. Cheng, C. Wang, L. Feng, K. Yang and Z. Liu, *Chem. Rev.*, 2014, **114**, 10869–10939.
4 J. Zou, P. Wang, Y. Wang, G. Liu, Y. Zhang, Q. Zhang, J. Shao, W. Si, W. Huang and X. Dong, *Chem. Sci.*, 2019, **10**, 268–276.
5 X. Yang, D. Wang, J. Zhu, L. Xue, C. Ou, W. Wang, M. Lu, X. Song and X. Dong, *Chem. Sci.*, 2019, **10**, 3779–3785.
6 J. Yang, Y. Shang, Y. Li, Y. Cui and X. B. Yin, *Chem. Sci.*, 2018, **9**, 7210–7217.
7 S. S. Lucky, K. C. Soo and Y. Zhang, *Chem. Rev.*, 2015, **115**, 1990–2042.
8 T. H. Foster and L. Gao, *Radiat. Res.*, 1992, **130**, 379–383.
9 J.-N. Liu, W. Bu and J. Shi, *Chem. Rev.*, 2017, **117**, 6160–6224.
10 X. Yang, Y. Yang, F. Gao, J.-J. Wei, C.-G. Qian and M.-J. Sun, *Nano Lett.*, 2019, **19**, 4334–4342.

11 D. Tao, L. Feng, Y. Chao, C. Liang, X. Song, H. Wang, K. Yang and Z. Liu, *Adv. Funct. Mater.*, 2018, **28**, 1804901.
12 H. Cheng, J.-Y. Zhu, S.-Y. Li, J.-Y. Zeng, Q. Lei, K.-W. Chen, C. Zhang and X.-Z. Zhang, *Adv. Funct. Mater.*, 2016, **26**, 7847–7860.
13 C. Huang, W. T. Chia, M. F. Chung, K. J. Lin, C. W. Hsiao, C. Jin, W.-H. Lim, C.-C. Chen and H.-W. Sung, *J. Am. Chem. Soc.*, 2016, **138**, 5222–5225.
14 I. Roy, T. Y. Ohulchanskyy, H. E. Pudavar, E. J. Bergey, A. R. Oseroff, J. Morgan, T. J. Dougherty and P. N. Prasad, *J. Am. Chem. Soc.*, 2003, **125**, 7860–7865.
15 D. K. Chatterjee, L. S. Fong and Y. Zhang, *Adv. Drug Delivery Rev.*, 2008, **60**, 1627–1637.
16 Y. Cao, T. Wu, K. Zhang, X. Meng, W. Dai, D. Wang, H. Dong and X. Zhang, *ACS Nano*, 2019, **13**, 1499–1510.
17 L. Teng, G. Song, Y. Liu, X. Han, Z. Li, Y. Wang, S. Huan, X.-B. Zhang and W. Tang, *J. Am. Chem. Soc.*, 2019, **141**, 13572–13581.
18 W. Fan, W. Bu, B. Shen, Q. He, Z. Cui, Y. Liu, Y. Zhang, K. Zhao and J. Shi, *Adv. Mater.*, 2015, **27**, 4155–4161.
19 Z. Ma, X. Jia, J. Bai, Y. Ruan, C. Wang, J. Li, M. Zhang and X. Jiang, *Adv. Funct. Mater.*, 2017, **27**, 1604258.
20 Y. Liu, K. Ai and L. Lu, *Chem. Rev.*, 2014, **114**, 5057–5115.
21 W. Cheng, X. Zeng, H. Chen, Z. Li, W. Zeng, L. Mei and Y. Zhao, *ACS Nano*, 2019, **13**, 8537–8565.
22 F. Shieh, S.-C. Wang, C. Yen, C.-C. Wu, S. Dutta, L.-Y. Chou, J. V. Morabito, P. Hu, M.-H. Hsu, K. C.-W. Wu and C.-K. Tsung, *J. Am. Chem. Soc.*, 2015, **137**, 4276–4279.
23 Y.-N. Wu, M. Zhou, B. Zhang, B. Wu, J. Li, J. Qiao, X. Guan and F. Li, *Nanoscale*, 2014, **6**, 1105–1112.
24 H. Wang, Y. Chen, H. Wang, X. Liu, X. Zhou and F. Wang, *Angew. Chem., Int. Ed.*, 2019, **58**, 7380–7384.
25 Z. Fang, J. P. Dürholt, M. Kauer, W. Zhang, C. Lochenie, B. Jee, B. Albada, N. Metzler-Nolte, A. Pöppl, B. Weber, M. Muhler, Y. Wang, R. Schmid and R. A. Fischer, *J. Am. Chem. Soc.*, 2014, **136**, 9627–9636.
26 W. Zhang, Y. Liu, G. Lu, Y. Wang, S. Li, C. Cui, J. Wu, Z. Xu, D. Tian, W. Huang, J. S. DuCheneu, W. D. Wei, H. Chen, Y. Yang and F. Huo, *Adv. Mater.*, 2015, **27**, 2923.
27 H. Cheng, J.-Y. Zhu, S.-Y. Li, J.-Y. Zeng, Q. Lei, K.-W. Chen, C. Zhang and X.-Z. Zhang, *Adv. Funct. Mater.*, 2016, **26**, 7847–7860.
28 M. S. Shim and Y. Xia, *Angew. Chem., Int. Ed.*, 2013, **52**, 6926–6929.
29 H. Chen, J. Tian, W. He and Z. Guo, *J. Am. Chem. Soc.*, 2015, **137**, 1539–1547.
30 H. Zheng, Y. Zhang, L. Liu, W. Wan, P. Guo, A. M. Nyström and X. Zou, *J. Am. Chem. Soc.*, 2016, **138**, 962–968.
31 F. Lyu, Y. Zhang, R. N. Zare, J. Ge and Z. Liu, *Nano Lett.*, 2014, **14**, 5761–5765.
32 K. Liang, R. Ricco, C. M. Doherty, M. J. Styles, S. Bell, N. Kirby, S. Mudie, D. Haylock, A. J. Hill, C. J. Doonan and P. Falcaro, *Nat. Commun.*, 2015, **6**, 7240.
33 L. Zhao, Y. Liu, R. Chang, R. Xing and X. Yan, *Adv. Funct. Mater.*, 2019, **29**, 1806877.
34 Z. Sheng, D. Hu, M. Zheng, P. Zhao, H. Liu, D. Gao, P. Gong, G. Gao, P. Zhang, Y. Ma and L. Cai, *ACS Nano*, 2014, **8**, 12310–12322.
35 Z. Sheng, D. Hu, M. Xue, M. He, P. Gong and L. Cai, *Nano-Micro Lett.*, 2013, **5**, 145–150.

